

Fabrication and Field-Emission Performance of Zinc Sulfide Nanobelt Arrays

Fang Lu,[†] Weiping Cai,^{*,†} Yugang Zhang,[†] Yue Li,^{†,‡} and Fengqiang Sun[†]

Key Laboratory of Materials Physics, Anhui Key Lab of Nanomaterials and Nanotechnology, Institute of Solid State Physics, Chinese Academy of Sciences, Hefei 230031, P. R. China

Sung Hwan Heo[‡] and Sung Oh Cho[‡]

Department of Nuclear and Quantum Engineering, Korea Advanced Institute of Science and Technology, 373-1 Guseong, Yuseong, Daejeon, Republic of Korea

Received: June 17, 2007; In Final Form: July 8, 2007

Large-scale, well-aligned, and oriented wurtzite ZnS nanobelt arrays have been synthesized by a simple template-free solvothermal reaction and subsequent heat-treatment process. The ZnS nanobelts grow along the [0001] direction perpendicularly on a zinc substrate, which have a thickness of about 30 nm, widths of several hundreds of nanometers, and uniform length up to 4 μm . The selection of Zn foil as the substrate is crucial for the formation of ZnS nanostructured arrays. The concentration of Zn ions, the pH value in the initial precursor solution, and the reaction temperature also have an important influence on the morphology of the final arrays. The formation of the nanobelt arrays are attributed to the structural compatibility of the substrate with ZnS and the growth-rate-dependence of morphology. Importantly, such nanostructured arrays show good field-emission properties with low turn-on fields (3.8 $\text{V}\mu\text{m}^{-1}$) and high field-enhancement factors (1839). This is attributed to the top edges and corners of the free-standing and well-aligned nanobelts, suitable number density of emitters, and good electric contact of the nanobelts with the conducting substrate where they grow. This well-aligned ZnS nanobelt array is expected to be the promising candidate for various field-emission applications, such as flat-panel displays and other vacuum microelectronic devices.

1. Introduction

Zinc sulfide (ZnS) is an important semiconductor with a large exciton binding energy (40 meV) and a small Bohr radius (2.4 nm), which has been considered to be a promising material for ultraviolet (UV)-light-emitting diodes and injection lasers,¹ phosphors in cathode-ray tube and flat-panel displays,² and infrared (IR) windows.³ In recent years, much attention has been focused on the synthesis of various ZnS nanostructures including nanorods,⁴ nanowires,⁵ nanotubes,⁶ and nanobelts.⁷ Among those, the nanobelt represents a special geometrical shape, in contrast to the other one-dimensional (1D) nanostructures such as nanowires and nanotubes with cylinder geometries, and has stimulated extensive research interest. The ribbon-like nanostructures have been expected to be important building blocks for nanodevices and offer exciting opportunities for both fundamental research and technological applications.⁸ Therefore, they have been synthesized in some materials, especially oxides.⁹ The ZnS nanobelts or nanoribbons have also been obtained mostly by the vapor-phase process.¹⁰ For instance, Wang et al. reported the synthesis of wurtzite-structured ZnS nanobelts based on thermal evaporation of ZnS powders at high temperatures.^{7a} Jiang et al. introduced a hydrogen-assisted thermal evaporation method to fabricate ZnS nanoribbons.^{7b} Commonly, these synthetic strategies need relatively rigid experimental conditions and sophisticated equipments. Comparatively, a solution-based approach has the advantages of mild synthetic conditions and

simple manipulation. Recently, Yao et al. prepared flower-like ZnS nanobelts by a low-temperature solution synthesis route.¹¹ However, all of the reported ZnS nanobelts were distributed randomly in powder form.

Many possible applications of 1D nanomaterials require the formation of well-aligned arrays to accentuate the anisotropy and satisfy the criteria of device design. The nanobelt arrays of some materials, such as ZnO,¹² SnO₂,¹³ CuO,¹⁴ and so forth, have been synthesized and studied extensively because of their high surface/volume ratio and special geometry. Such arrays have exhibited good field-emission (FE) and sensing properties.^{14b} However, until now only the fabrication of the nanobelt arrays of oxide semiconductors is reported while the synthesis of sulfide nanobelt arrays is still a challenge.

Recently, we have prepared the large-scale well-aligned wurtzite ZnS nanobelt arrays vertically on a zinc foil by a simple solvothermal reaction and subsequent heat treatment. Importantly, such nanostructured arrays show the very-good FE property with very-low turn-on fields and high field-enhancement factor, which should be potentially applicable to various field-emission-based devices.¹⁵ These well-aligned ZnS nanobelt arrays are expected to be promising candidates for various FE applications, such as flat-panel displays and other vacuum microelectronic devices. Partial preliminary results about the synthesis of the nanobelt array and its FE properties were reported previously.¹⁵ In this article, we will report the systematic and deep works about the fabrication and field-emission performance of the zinc sulfide nanobelt array. We focus mainly on the factors influencing the formation of the ZnS nanobelt array (such as substrate, zinc ion concentration in precursor solution, pH value in precursor solution, and

* To whom correspondence should be addressed. E-mail: wpcai@issp.ac.cn.

[†] Chinese Academy of Sciences.

[‡] Korea Advanced Institute of Science and Technology.

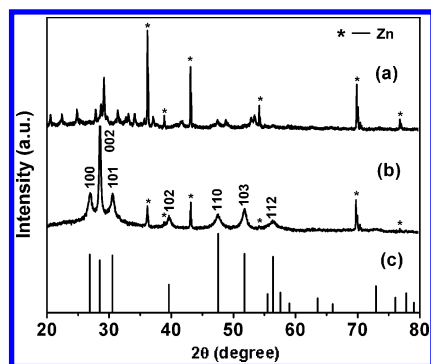


Figure 1. XRD patterns for the reacted products on a Zn substrate. (a) Products after solvothermal reaction at 160 °C for 10 h. (b) Subsequent heating at 250 °C for $\frac{1}{2}$ h under a vacuum. (c) Standard XRD pattern for ZnS powders from the Joint Committee on Power Diffraction Standards, JPCDS card file (no. 36-1450).

reaction temperature) and its formation mechanisms (including the growth-rate dependence of morphology and the structural compatibility of the substrate with the compound), in addition to FE properties.

2. Experimental Section

2.1. Preparation. In our experiments, all chemicals were of analytical grade and were used as received without further purification. Zinc foils (99.99%, Aldrich) were ultrasonically washed in absolute ethanol before use. Typically, Zn (CH_3COO) $_2 \cdot 2\text{H}_2\text{O}$ (0.5 mmol) and CS (NH_2) $_2$ (1 mmol) were dissolved in deionized water to form a 10.0 mL solution, and its pH value was adjusted to 10 by dropping 3 M NaOH solution. Then, 30 mL of ethylenediamine (EDA) was added while stirring continued. Afterward, the mixture was transferred into a 50-mL Teflon-lined autoclave, followed by immersing a piece of zinc foil ($1 \times 1 \text{ cm}^2$) in the reactant solution. The autoclave was sealed, heated to 160 °C for 10 h, and then allowed to cool to room temperature. The foil covered with reaction products was collected from the solution, rinsed with distilled water and absolute ethanol, and dried under vacuum ($\sim 10^{-3}$ Torr) at 70 °C for 5 h. Finally, the products were heated at 250 °C for $\frac{1}{2}$ h in a vacuum ($\sim 10^{-3}$ Torr) furnace to form ZnS.

2.2. Characterization and Measurements. The products were characterized by X-ray diffraction (XRD, X'Pert Pro MPD), a field-emission scanning electron microscope (FESEM, Sirion 200), and a high-resolution transmission electron microscope (HRTEM, JEOL 2010). The FE measurements were performed in a vacuum chamber at a pressure of 5×10^{-7} Pa at room temperature in a two-parallel-plate configuration. The sample on the Zn substrate (foil) was attached to a stainless-steel plate using conducting glue as the cathode together with the other as the anode. The emission current was monitored with a Keithley 485 picoammeter.

3. Results and Discussion

3.1. Structural Characterization of ZnS Nanobelt Arrays.

The XRD patterns of the products on the Zn substrate are shown in Figure 1 in which the standard diffraction of hexagonal (wurtzite) ZnS powders is also given (bottom). The pattern for the products after solvothermal reaction at 160 °C for 10 h (curve a in Figure 1) can be indexed as orthorhombic Zn-sulfur-ethylenediamine [$\text{ZnS}(\text{EDA})_{0.5}$] except the signals of Zn metal from the substrate, compared with the XRD pattern presented by Ouyang et al.¹⁶ Subsequent heating at 250 °C under a vacuum leads to the thermal decomposition of the $\text{ZnS}(\text{EDA})_{0.5}$ and

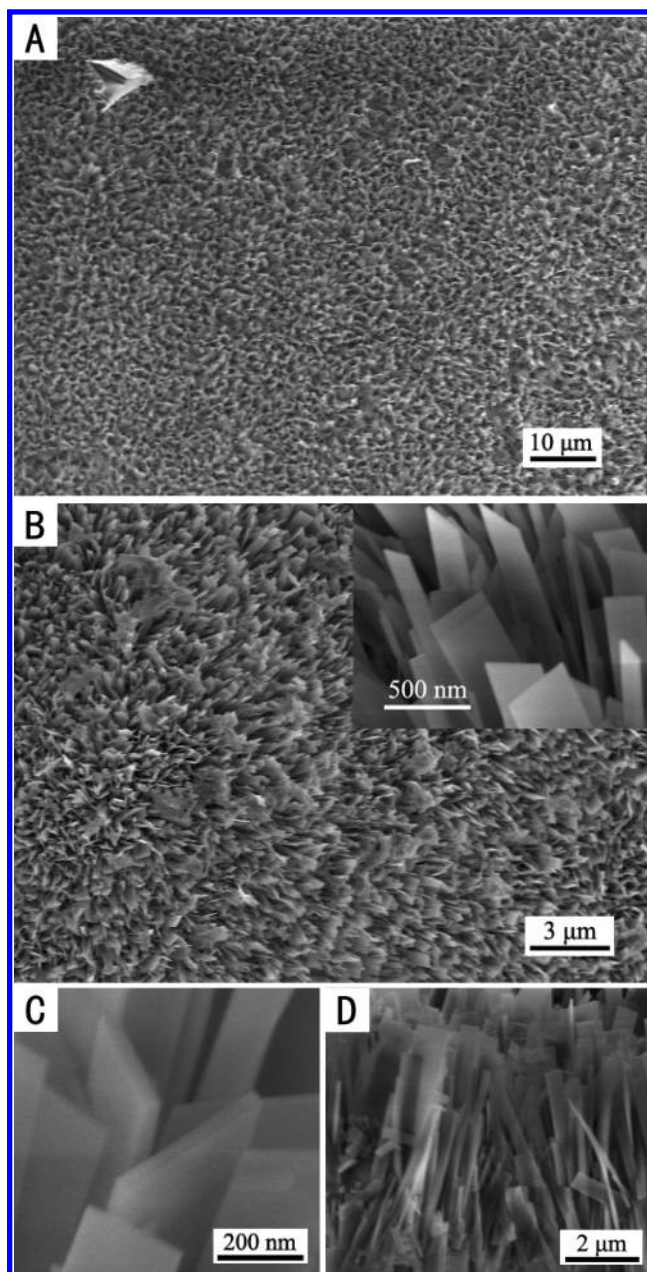


Figure 2. FESEM images of ZnS nanobelt arrays synthesized at 160 °C for 10 h ($[\text{Zn}^{2+}] = 12.5 \text{ mM}$, pH = 10) and after heating at 250 °C for $\frac{1}{2}$ h under a vacuum. (A) Low-magnification image. (B) Local magnified image in A; the inset in B: higher-magnification image in B. (C) Enlarged image near the top part of the belts. (D) Cross-section image.

formation of wurtzite ZnS, as shown in curve b of Figure 1, in which all peaks are in agreement with wurtzite ZnS (JCPDS Card 36-1450), except the signals of Zn metal from the substrate. In addition, the strongest peak for the final sample corresponds to (002), whereas that of the standard ZnS powders is (100), indicating that the ZnS on the substrate has significantly preferred orientation in the direction of [0001].

Figure 2 clearly shows the morphology of the final product. The Zn foil is covered with uniform and dense ZnS products (Figure 2A). The local magnification of FESEM images exhibits that the products are composed of vertically standing nanobelts (Figure 2B and its inset) and each of them has a clear rectangle on their top section (Figure 2C). These nanobelts are 300–500 nm in width, up to 4 μm in length, and about 30 nm in thickness, which are aligned in a dense array and approximately perpen-

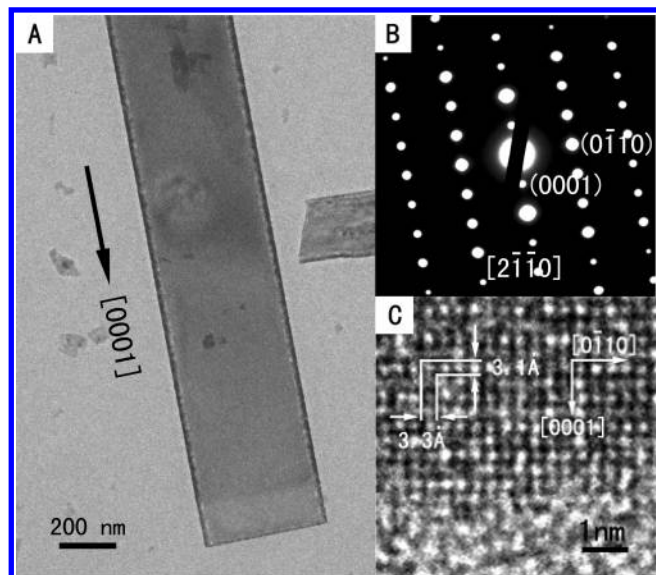


Figure 3. TEM image (A), SEAD pattern recorded along the $[2110]$ zone (B), and HRTEM image (C) of a single ZnS nanobelt.

dicular to the substrate surface (Figure 2D). These results are in agreement with our previous reports¹⁵

Transmission electron microscopic (TEM) examination has revealed that the nanobelts have a uniform width over their entire lengths, as typically illustrated in Figure 3A. Selected-area electron diffraction (SAED) shows that the nanobelts are well-crystallized single crystals of wurtzite ZnS (see Figure 3B). The nanobelt grows along $[0001]$, with side surfaces (0110) and the belt-planar surfaces (2110) . The HRTEM image (Figure 3C) exhibits well-resolved 2D lattice fringes with spacings of 3.1 and 3.3 Å, which are in good agreement with the spacings of the $\{0001\}$ and $\{0110\}$ planes in wurtzite ZnS, respectively. These further confirmed that each nanobelt is single crystal and the c -axial direction is the fastest growth direction.

3.2. Factors Influencing Formation of the ZnS Nanobelt Arrays. The selection of Zn foil as a substrate is crucial for the formation of such ZnS nanostructured arrays. In addition, the concentrations of zinc ions, the pH value in the precursor solution, and the reaction temperature are also important to the morphology and nanobelt size of the final arrays.

3.2.1. Substrate. It has been found that the Zn foil as a substrate is requisite for the formation of the ZnS (EDA)_{0.5} and thus ZnS nanostructured arrays. If we use a Si substrate, instead of Zn foil, and keep the other experimental parameters unchanged, then only quadrate platelet-like nanocrystals with uneven sizes are obtained, which are initially formed in the solution followed by depositing on the surface of the substrate in randomly distributed powder form, rather than nanostructured arrays with good alignment, as illustrated in Figure 4A. Alternatively, we have closely observed the morphology on the edge region of the sample with the Zn substrate (corresponding to the sample shown in Figure 2) and found the important information about the growth of nanobelts, which could exhibit the role of Zn foil more clearly, as shown in Figure 4B. The nanobelts evidently grow on the substrate despite the poor alignment due to the edge region.

3.2.2. Zinc Ion Concentration in Precursor Solution. Figure 5 shows the morphology of the products on the Zn foils synthesized with different concentrations of Zn^{2+} in precursor

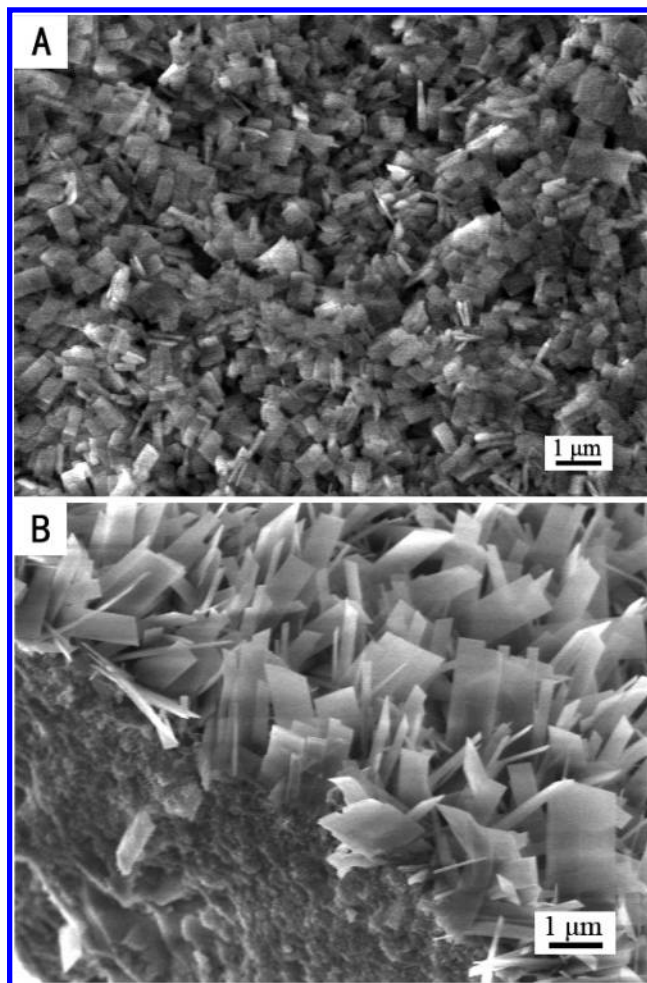


Figure 4. FESEM images of (A) the products obtained using Si foil as the substrate keeping other experimental parameters. (B) Products grown on the edge region of the Zn substrate corresponding to the sample shown in Figure 2.

solution. When no zinc acetate is added into the initial solution, nanosheets are formed nearly vertically standing on the Zn substrate, showing network-like morphology from top view (Figure 5A). This demonstrates that the Zn foil can also provide Zn^{2+} source during reaction. When increasing the Zn^{2+} concentration to 2 and 4 mM by addition of zinc acetate, the morphologies of the obtained products are still similar to that without the addition of zinc acetate, showing intermeshed nanosheets vertically on the Zn foil, as illustrated in Figure 5B and C. If the Zn^{2+} concentration reaches up to 8 and 10 mM, then the morphology evolves from the net-like to more-dense arrangement of nanosheets (from top view), as shown in Figure 5D and E. Further increasing the concentration higher than 10 mM (e.g., 12.5 mM) leads to the nanobelt array as shown in Figure 2. When the Zn^{2+} concentration is increased further (e.g., 15 mM), in addition to the nanobelt array growing on the Zn substrate, some area on the top of the sample are covered with many randomly distributed ZnS aggregates precipitated from the solution due to the homogeneous nucleation occurring in the solution, as displayed in Figure 5F. Here it should be mentioned that XRD measurements show the same products for the samples from the precursor solutions with different Zn^{2+} concentrations (similar to the pattern shown in Figure 1). All of these indicate that the appropriate Zn^{2+} concentration in the reactant solution is vital for the formation of ZnS (EDA)_{0.5} and thus ZnS nanobelt arrays.

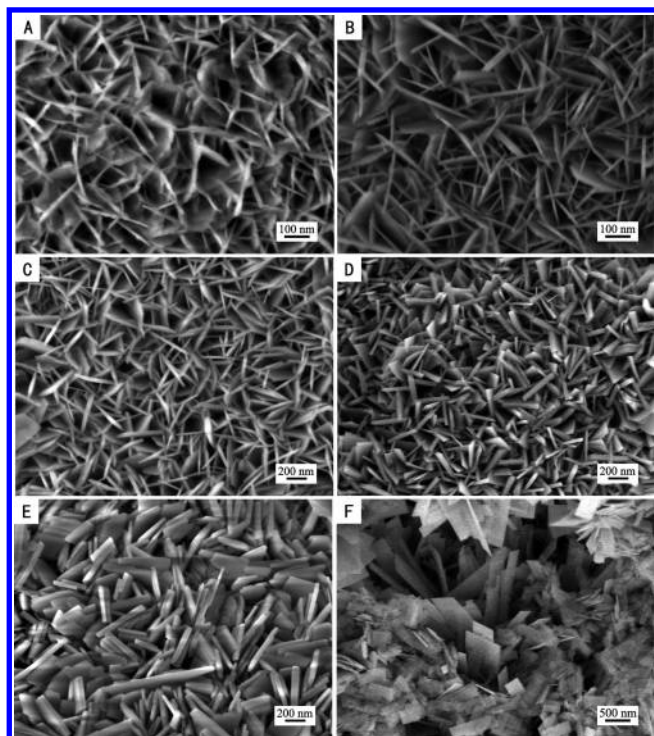


Figure 5. FESEM images of the products on the Zn foils synthesized from the precursor solutions with different zinc acetate or Zn^{2+} concentrations. (A) 0 mM, (B) 2 mM, (C) 4 mM, (D) 8 mM, (E) 10 mM, and (F) 15 mM.

3.2.3. pH Value in the Precursor Solution. Further experiments have demonstrated that the OH^- concentration or pH value in the reactant solution has an important effect on the morphologies of the products. Figure 6 shows the morphologies of the products synthesized from the solution ($[\text{Zn}^{2+}] = 12.5$ mM) with different pH values from 4 to 12 controlled by dropping NaOH.

Without the addition of NaOH (pH = 4), nearly vertical sheet-like ZnS nanocrystals with irregular shapes are formed on the substrate (Figure 6A). When the pH value increases up to 8, the ZnS nanocrystals evolve to the vertically standing quadrate nanosheet in a high-number-density arrangement (Figure 6B). The TEM and SEAD examination show that all of the ZnS nanosheets, for the sample shown in Figure 6B, are of nearly square shape with micrometer size and single-crystal structure (see Figure 7A and B). The corresponding HRTEM observation (Figure 7C) exhibits well-resolved 2D lattice fringes with the spacings of 3.1 and 3.3 Å, which are in good agreement with the interplanar spacings of $\{0001\}$ and $\{0110\}$ planes, respectively. The 2D nanosheets grow preferentially along the directions of both $\langle 0110 \rangle$ and $\langle 0001 \rangle$ with nearly equal growth rates. Only when pH = 10 or higher, the ZnS nanobelt arrays are formed with good alignment, where each belt possesses a regularly rectangular top section (Figures 2B or 6C). These results indicate that the morphologies of the final products on the zinc substrate are sensitive to the pH value in the precursor solution.

3.2.4. Reaction Temperature. The reaction temperature is also a vital factor for the morphology of $\text{ZnS}(\text{EDA})_{0.5}$ and thus ZnS nanostructures grown directly on the zinc foils. If the reaction temperature decreases down to 130 °C ($[\text{Zn}^{2+}] = 12.5$ mM, pH = 10 in the solution), then vertically aligned nanoplatelets, instead of nanobelts, are formed, as displayed in Figure 8A. In contrast to the sample synthesized at 160 °C (see Figure 2B), the arrangement of the nanoplatelets is more compact. When

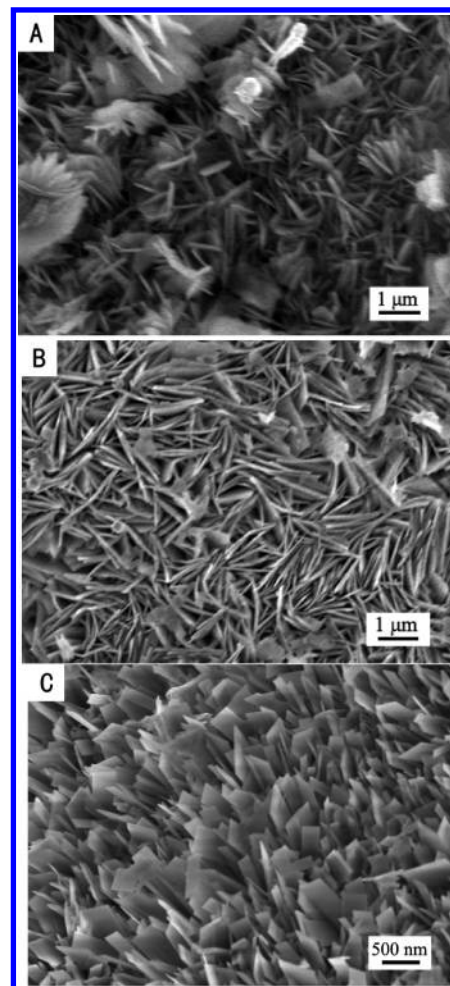


Figure 6. FESEM images of the products synthesized from the precursor solutions with different pH values (see the text): (A) 4, (B) 8, and (C) 12. (The concentration of Zn^{2+} is fixed at 12.5 mM.)

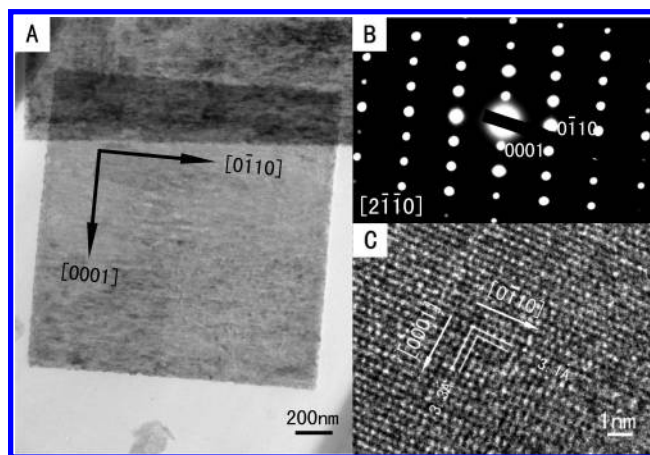


Figure 7. Microstructure analysis of a wurtzite ZnS nanosheet corresponding to the sample shown in Figure 6B. (A) TEM image; (B) SEAD pattern recorded along the $[2110]$ zone, and (C) HRTEM image.

the reaction temperature increases up to 180 °C, the ZnS nanobelts are not erectly standing on the zinc substrate, and the top parts of many nanobelts are bent, as shown in Figure 8B.

3.3. Formation of ZnS Nanobelt Arrays. Formation of wurtzite ZnS nanocrystals originates from the thermal decom-

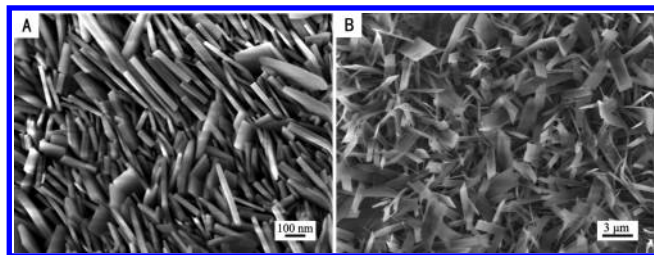
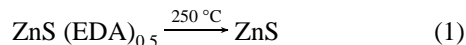


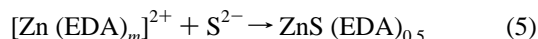
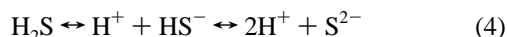
Figure 8. FESEM images of the products obtained on the Zn foils at different reaction temperatures for 10 h ($[\text{Zn}^{2+}] = 12.5 \text{ mM}$, $\text{pH} = 10$). (A) 130°C , (B) 180°C .

position of the transitional reaction product $\text{ZnS (EDA)}_{0.5}$ at subsequent heating at 250°C , or the reaction



and its shape-transferring or inheritance.¹⁷

In our case, the Zn foil serves as both a substrate and a zinc source. Zinc ions were provided by not only $\text{Zn (CH}_3\text{COO)}_2 \cdot 2\text{H}_2\text{O}$ in the precursor solution but also the oxidation of metal zinc substrate. In the EDA-sufficient precursor solution, Zn^{2+} reacts with thiourea to form $\text{ZnS (EDA)}_{0.5}$ molecules during heating in the autoclave at 160°C by the reactions^{17,18}



With the increase of $\text{ZnS (EDA)}_{0.5}$ concentration in the solution, $\text{ZnS (EDA)}_{0.5}$ crystal nuclei will heterogeneously be formed on the Zn substrate because of the lower energy barrier than that in the solution. In general, the faces perpendicular to the fast direction of growth have smaller surface areas and the faces perpendicular to the slow growing direction thus dominate the morphology.¹⁹ For $\text{ZnS (EDA)}_{0.5}$, there are two preferential growth directions, $[0001]$ and $[01\bar{1}0]$.¹⁷ The final shape of $\text{ZnS (EDA)}_{0.5}$ nanocrystal, that is belt or square sheet, depends on the relative growth rate of the $[0001]$ and $[01\bar{1}0]$ directions. In our case, the growth rate of the $[0001]$ direction is faster than

that of $[01\bar{1}0]$. Thus, the belt-like morphology was produced. Obviously, only the nuclei with the (0001) plane parallel to the substrate are allowed to grow freely because the growth of other plane-oriented nuclei will be kinetically retarded and cannot grow very long because of limited space²⁰ (as seen in Figure 2D). Consequently, well-aligned nanobelt arrays are formed nearly vertically on the substrate, as illustrated schematically in Figure 9.

3.4. Effects of Experimental Parameters. **3.4.1. Growth-Rate Dependence of Morphology.** In principle, final morphology of the $\text{ZnS (EDA)}_{0.5}$ nanocrystal depends on the relative growth rates between the two preferential directions, $[0001]$ and $[01\bar{1}0]$,^{16,17} as illustrated schematically in Figure 9. When the growth of crystal is slow, the difference between the growth rates along $[0001]$ and $[01\bar{1}0]$ is small. In this case, $V_{[0001]} \approx V_{[01\bar{1}0]}$ and nanosheet arrays will be formed (see flowchart I in Figure 9). Otherwise, if the growth of crystal is fast, the difference of the growth rates along these two directions will be significant or the growth rate along $[0001]$ will be much faster than that along $[01\bar{1}0]$, that is, $V_{[0001]} \ll V_{[01\bar{1}0]}$, leading to the formation of nanobelt arrays (see flowchart II in Figure 9). Obviously, the growth rate of the $\text{ZnS (EDA)}_{0.5}$ crystal is associated with the Zn^{2+} concentration and the pH value in the solution in addition to the reaction temperature.

When the Zn^{2+} concentration is relatively low, resulting in slow growth of the crystal, the difference between the growth rates along $[0001]$ and $[01\bar{1}0]$ is small or $V_{[0001]} \approx V_{[01\bar{1}0]}$. In this case, we can only observe a nanosheet array (see Figure 5A–E). Only a high enough Zn^{2+} concentration, leading to high enough growth rates or $V_{[0001]} \gg V_{[01\bar{1}0]}$, induces the formation of the nanobelt arrays (see Figure 2B). When the concentration is too high, however, homogeneous nucleation will occur in solution. So some areas on the top of the sample are covered with many randomly distributed ZnS aggregates that precipitated from the solution, in addition to the nanobelt array growing on the Zn substrate, as displayed in Figure 5F.

For the pH or $[\text{OH}^-]$ concentration of in the solution, the high value accelerates the thermal hydrolysis of thiourea (e.g., $\text{H}_2\text{S} + 2\text{OH}^- \rightarrow \text{S}^{2-} + 2\text{H}_2\text{O}$, $\text{SH}^- + \text{OH}^- \rightarrow \text{S}^{2-} + \text{H}_2\text{O}$)¹⁸ and greatly increases the $[\text{S}^{2-}]$ concentration. This will lead to the fast formation of $\text{ZnS (EDA)}_{0.5}$ according to reaction 5 and a high growth rate of the crystal. As discussed above, the high growth rate will correspond to $V_{[0001]} > V_{[01\bar{1}0]}$, which is beneficial to the formation of the belt-like morphology of the

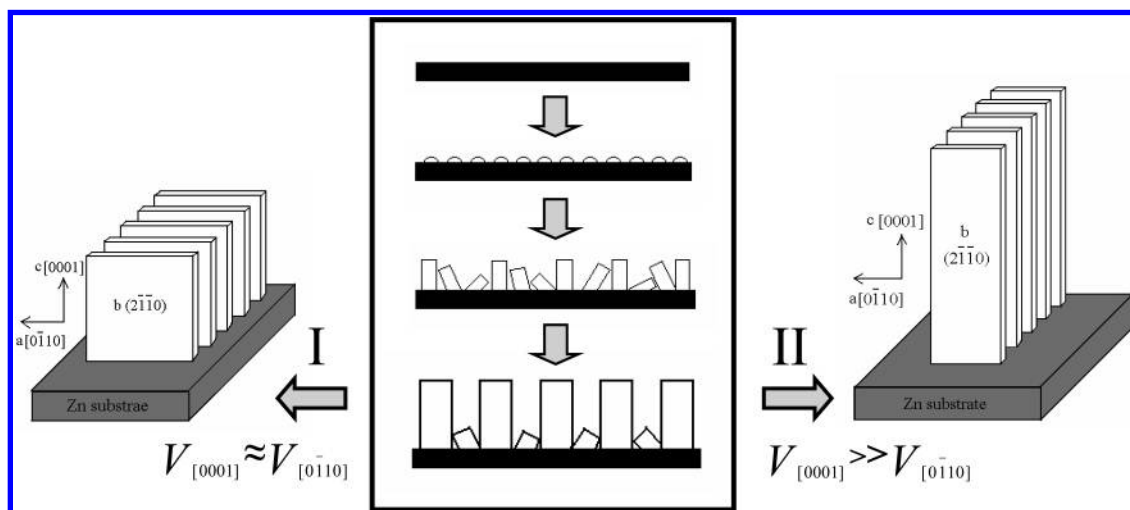


Figure 9. Schematic illustration for the growth mechanism of the $\text{ZnS(EDA)}_{0.5}$ nanosheet array (II) and nanobelt array (I).

ZnS (EDA)_{0.5} nanocrystal, which is similar to the H₂O₂-assisted growth of ZnO nanorod arrays on Zn foils.^{21a} Alternatively, the sufficient existence of [OH⁻] makes it possible to form such molecular transport complexes with negative charge as [Zn (EDA)_m (H₂O)_k (OH⁻)_l]^{(l-2m)-}. They can adsorb on the positive polar face of (0001) because of the electrostatic force and preferentially transport Zn²⁺ to this growing crystal plane, leading to faster growth along the [0001] direction.²² It should be pointed out that the effects of [OH⁻] seem to be more complicated, and further study is being performed to improve the understanding of the exact role of [OH⁻] concentration in the formation of ZnS (EDA)_{0.5} nanobelt arrays.

Similarly, a high reaction temperature will increase the growth rate of the crystal and hence the ratio of $V_{[0001]}/V_{[0\bar{1}10]}$, which is beneficial to formation of the nanobelts. However, too high of a temperature (say, 180 °C) will induce growth that is too fast, leading to the very-long standing nanobelts, in the same reaction time, with poor alignment and bent top parts (see Figure 8B).

As for the role of the Zn substrate, it can mainly be attributed to the structural compatibility of metal with the corresponding compound.

3.4.2. Structural Compatibility of Substrate with Compound. It is known that structural compatibility of a metal with its corresponding compound exists. It has been reported that such compatibility led to the formation of the nanostructured arrays of chalcogenides on the their metal substrates by solution-phase routes,²¹ such as oriented nanostructured nickel sulfides,²³ copper and silver tellurides,²⁴ and oriented lead telluride nanotubes and nanowires.²⁵ So, it is reasonable to suggest that, in our case, the Zn substrate provides such structural compatibility for ZnS (EDA)_{0.5}, leading to preferential nucleation on the substrate. Additionally, the Zn substrate can also continuously supply the zinc source during the reaction because of the oxidation, which induces a gradient of the Zn²⁺ concentration from the substrate surface to the bulk solution. At the same time, the eroded surface of the zinc substrate would be of higher chemical activity. These are all beneficial to preferential nucleation of ZnS (EDA)_{0.5} on the substrate. Obviously, the Si substrate does not possess such characteristics as Zn; that is, preferential nucleation of ZnS (EDA)_{0.5} cannot occur on the Si substrate. Finally, only platelet-like nanocrystals with random distributions are obtained because of the homogeneous nucleation in the solution and subsequent deposition on the substrate, as shown in Figure 4A.

3.5. Field-Emission Properties. More interestingly, such ZnS nanobelt arrays show good FE property because of its structure, in contrast to the bulk ZnS that is insignificant. Figure 10A shows the dependence of the emission current density, J , on the applied electric field E ($E = V/d$, where d is the anode-sample distance) at two anode-sample distances, 200 and 300 μm , for the ZnS nanobelt array shown in Figure 2. The turn-on fields are measured to be about 5.0 and 3.8 $\text{V}/\mu\text{m}$ for anode-sample distances of 200 and 300 μm , respectively, corresponding to a current density of 10 $\mu\text{A}/\text{cm}^2$. Although there is no available reported data for ZnS, the turn-on field values in this work for the ZnS nanobelt array are comparable to those observed for many other types of field emitters. Such a low turn-on field is close to those observed in some good field emitters, such as, single-walled carbon nanotubes (1.5–4.5 $\text{V}/\mu\text{m}$),²⁶ needle-shaped SiC nanowires ($\sim 5 \text{ V}/\mu\text{m}$),²⁷ or hierarchical wurtzite AlN nanoarchitectures (2.45–3.76 $\text{V}/\mu\text{m}$).²⁸ And it is much lower than those of Cu₂S nanowires,²⁹ MoS₂ nanoflowers,³⁰ taper-like Si nanowires,³¹ Si nanocone arrays,³² ZnO nanowires,³³ MoO₃ nanobelts,³⁴ WO₃- δ nanowire networks,³⁵ GaN

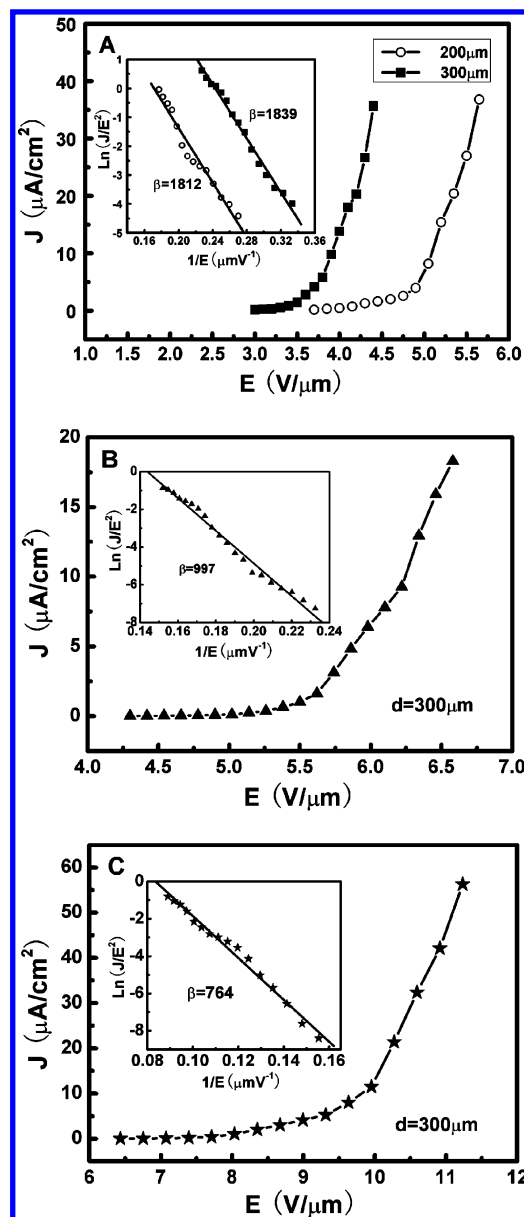


Figure 10. Field-emission measurements of ZnS nanostructured arrays. (A) Field-emission J - V curves and corresponding FN plots (inset) for the ZnS nanobelt array shown in Figure 2 at two anode-sample distances of 200 and 300 μm . (B) and (C) Field-emission J - V curves and corresponding FN plots (insets) for the samples shown in Figure 8A and B, respectively, at a fixed anode-sample distance of 300 μm .

nanowires,³⁶ and most AlN nanostructures.³⁷ It indicates that the obtained ZnS nanobelt array is, in fact, an excellent field emitter.

The low turn-on field for ZnS nanobelt arrays could be attributed to the sharp corners and edges of belts, the suitable emitter density, and the well-aligned morphologies. Additionally, the direct growth of the nanobelts on the conducting metal substrate can ensure a good electrical contact, which also contributes to such a low turn-on field observed here.³⁸ The results in Figure 10A can be described by Fowler-Nordheim (FN) theory³⁹

$$J = (AE^2\beta^2/\Phi) \exp(-B\Phi^{3/2}/E\beta) \quad (6)$$

where Φ is the work function of emitter materials (in eV), A and B are constants, corresponding to 1.56×10^{-10} (AV^{-2}eV) and 6.83×10^3 ($\text{V eV}^{-3/2} \mu\text{m}^{-1}$), respectively, and β is the

field-enhancement factor indicating the degree of the FE enhancement of any tip shape on a planar surface. The inset in Figure 10A shows FN plots of $\ln(J/E^2)$ versus E^{-1} corresponding to Figure 10A. The FN plots corresponding to different anode–sample separations show a similar linear relationship within the measurement range, revealing that electron emission from these ZnS nanoarchitectures follows the FN's behavior, that is, electron tunneling through a potential barrier (FN mechanism).⁴⁰ On the basis of the slope of the $\ln(J/E^2) \sim E^{-1}$ plot and the work function of bulk ZnS (5.4 eV),⁴¹ β is estimated to be 1812 for $d = 200 \mu\text{m}$ and 1839 for $d = 300 \mu\text{m}$, respectively, which is high enough for various field-emission applications. The β factor is highly dependent on the geometrical shape and crystal structure of the emitter as well as the density of the emitting points. Such a high β value can be attributed to the geometrical features of the ZnS nanobelts, including high aspect ratios, nanosized sharp corners and edges on the top end of the belts, suitable number density of emitters, and alignment of these belts.

The analyses above have been confirmed by the further comparative experiments where the distance between the two electrodes was kept at $300 \mu\text{m}$, as illustrated in Figure 10B and C corresponding to the FE properties of the ZnS nanostructured arrays shown in Figure 8. The compactly arranged nanoplatelet array shown in Figure 8A exhibits a turn-on field of $6.2 \text{ V}/\mu\text{m}$ and a β value of 997, whereas the poorly aligned nanobelts shown in Figure 8B exhibit $10 \text{ V}/\mu\text{m}$ and 764, respectively. It is evident that both of them are worse than the nanobelt array in FE performance. The poor emission of the compactly arranged nanoplatelet array can be attributed to an electrostatic screening effect due to the proximity of neighboring emission units.⁴² For the poorly aligned nanobelts shown in Figure 8B, with most of the belt-planar surfaces exposed outward, the worse FE property would mainly be attributed to the deviation from the direction of the electric field for the emission due to the bent belt-shape, which is consistent with the results in many previous reports.^{34,43} Comparatively, the obtained ZnS nanobelt array, with a suitable number density of nanobelts and their vertically standing arrangement, exhibits excellent FE properties with a low turn-on field ($3.8 \text{ V}/\mu\text{m}$) and a high field-enhancement factor (1839). Obviously, better control of the emitter morphology and its number density by optimizing experimental parameters is requisite for future device applications.

4. Conclusions

In summary, large-scale and well-aligned ZnS nanobelt arrays have been synthesized successfully based on a simple template-free solvothermal strategy and a subsequent heat-treatment process. The nanobelts grow along the [0001] direction of ZnS perpendicularly on a zinc substrate, which have a thickness of about 30 nm, widths of several hundreds of nanometers, and uniform lengths up to $4 \mu\text{m}$. Further experiments have revealed that the selection of Zn foil as the substrate is crucial for the formation of ZnS nanostructured arrays because the Zn substrate can provide the structural compatibility and high active surface, and hence lead to preferential nucleation of ZnS (EDA)_{0.5} on the substrate. In addition, the concentrations of zinc ions, the pH value in the precursor solution, and the reaction temperature can determine the growth rate of the crystal or the difference between the growth rates along [0001] and [0110] and, hence, also have important influences on the morphology and nanobelt size of the final arrays. Importantly, such ZnS nanobelt arrays show good field-emission properties with a very-low turn-on

field ($3.8 \text{ V}/\mu\text{m}^{-1}$) and high field-enhancement factor (1839), due to the top edges and corners of the free-standing and well-aligned nanobelts, suitable number density of the emitters, and good electric contact of the nanobelts with the conducting substrate where they grow. This well-aligned ZnS nanobelt array is expected to be the promising candidate for various field-emission applications, such as flat-panel displays and other vacuum microelectronic devices.

Acknowledgment. This work was supported by the National Natural Science Foundation of China (Grant Nos. 50671100 and 50502032), the Major State research program of China “Fundamental Investigation on Micro–Nano Sensors and Systems based on BNI Fusion” (Grant No. 2006CB300402), and the Knowledge Innovation Program of the Chinese Academy of Sciences (Grant No. KJCX2-SW-W31).

References and Notes

- (1) Yamamoto, T.; Kishimoto, S.; Iida, S. *Phys. B* **2001**, 308, 916.
- (2) Bredol, M.; Merikhi, J. *J. Mater. Sci.* **1998**, 33, 471.
- (3) (a) Vacassy, R.; Scholz, S. M.; Dutta, J.; Hofmann, H.; Plummer, C. J. G.; Carrot, G.; Hilborn, J.; Akine, M. *Mater. Res. Soc. Symp. Proc.* **1998**, 501, 369. (b) Calandra, P.; Goffredi, M.; Turco Liveri, V. *Colloids Surf., A* **1999**, 160, 9.
- (4) Zhang, D.; Qi, L.; Cheng, H.; Ma, J. *J. Colloid Interface Sci.* **2002**, 246, 413.
- (5) (a) Jiang, Y.; Meng, X. M.; Liu, J.; Hong, Z. R.; Lee, C. S.; Lee, S. T. *Adv. Mater.* **2003**, 15, 1195. (b) Wu, Q. S.; Zheng, N. W.; Ding, Y. P.; Li, Y. D. *Inorg. Chem. Commun.* **2002**, 5, 671. (c) Jiang, X.; Xie, Y.; Lu, J.; Zhu, L.; He, W.; Qian, Y. T. *Chem. Mater.* **2001**, 13, 1213.
- (6) Yin, L. W.; Bando, Y.; Zhan, J. H.; Li, M. S.; Golberg, D. *Adv. Mater.* **2005**, 17, 1972.
- (7) (a) Ma, C.; Moore, D.; Li, J.; Wang, Z. L. *Adv. Mater.* **2003**, 15, 228. (b) Jiang, Y.; Meng, X. M.; Liu, J.; Xie, Z. Y.; Lee, C. S.; Lee, S. T. *Adv. Mater.* **2003**, 15, 323. (c) Li, Q.; Wang, C. R. *Appl. Phys. Lett.* **2003**, 83, 359. (d) Wang, Z. W.; Daemen, L. L.; Zhao, Y. S.; Zha, C. S.; Downs, R. T.; Wang, X. D.; Wang, Z. L.; Hemleys, R. J. *Nat. Mater.* **2005**, 4, 922.
- (8) (a) Comini, E.; Faglia, G.; Sberveglieri, G.; Pan, Z. W.; Wang, Z. L. *Appl. Phys. Lett.* **2002**, 81, 1869. (b) Hughes, W.; Wang, Z. L. *Appl. Phys. Lett.* **2003**, 82, 2886. (c) Arnold, M.; Avouris, P.; Pan, Z. W.; Wang, Z. L. *J. Phys. Chem. B* **2003**, 107, 659.
- (9) (a) Pan, Z. W.; Dai, Z. R.; Wang, Z. L. *Science* **2001**, 291, 1947. (b) Shi, W. S.; Peng, H. Y.; Wang, N.; Li, C. P.; Xu, L.; Lee, C. S.; Karish, R.; Lee, S. T. *J. Am. Chem. Soc.* **2001**, 123, 11095. (c) Dai, Z. R.; Gole, J. L.; Stout, J. D.; Wang, Z. L. *J. Phys. Chem. B* **2001**, 106, 1274. (d) Dai, Z. R.; Pan, Z. W.; Wang, Z. L. *J. Phys. Chem. B* **2002**, 106, 902. (e) Wang, Z. L. *Adv. Mater.* **2003**, 15, 432. (f) Xu, T. T.; Zheng, J. G.; Wu, N. Q.; Nicholls, A. W.; Roth, J. R.; Dikin, D. A.; Ruoff, R. S. *Nano Lett.* **2004**, 4, 963. (g) Gao, P. X.; Ding, Y.; Mai, W.; Hughes, W. L.; Lao, C. S.; Wang, Z. L. *Science* **2005**, 309, 1700.
- (10) (a) Zhu, Y. C.; Bando, Y.; Xue, D. F. *Appl. Phys. Lett.* **2003**, 82, 1769. (b) Li, Q.; Wang, C. R. *Appl. Phys. Lett.* **2003**, 83, 359.
- (11) Yao, W. T.; Yu, S. H.; Pan, L.; Li, J.; Wu, Q. S.; Zhang, L.; Jiang, J. *Small* **2005**, 1, 320.
- (12) Wen, X. G.; Fang, Y. P.; Pan, Q.; Yang, C. L.; Wang, J. N.; Ge, W. K.; Wong, K. S.; Yang, S. H. *J. Phys. Chem. B* **2005**, 109, 15303.
- (13) Chen, Y. J.; Li, Q. H.; Liang, Y. X.; Wang, T. H.; Zhao, Q.; Yu, D. P. *Appl. Phys. Lett.* **2004**, 85, 5682.
- (14) (a) Wen, X. G.; Zhang, W. X.; Yang, S. H. *Langmuir* **2003**, 19, 5898. (b) Chen, J.; Huang, N. Y.; Deng, S. Z.; She, J. C.; Xu, N. S. *Appl. Phys. Lett.* **2005**, 86, 151107.
- (15) Lu, F.; Cai, W. P.; Zhang, Y. G.; Li, Y.; Sun, F. Q.; Heo, Sung, H.; Cho, S. O. *Appl. Phys. Lett.* **2006**, 89, 231928.
- (16) Ouyang, X.; Tsai, T. Y.; Chen, D. H.; Huang, Q. J.; Cheng, W. H.; Clearfield, A. *Chem. Commun.* **2003**, 886.
- (17) (a) Yu, S. H.; Yoshimura, M. *Adv. Mater.* **2002**, 14, 296. (b) Deng, Z. X.; Wang, C.; Sun, X. M.; Li, Y. D. *Inorg. Chem.* **2002**, 41, 869. (c) Zhou, G. T.; Wang, X. C.; Yu, J. C. *Cryst. Growth Des.* **2005**, 5, 1761.
- (18) (a) Kuang, D. B.; Xu, A. W.; Fang, Y. P.; Liu, H. Q.; Frommen, C.; Fenske, D. *Adv. Mater.* **2003**, 15, 1747. (b) Engelken, R. D.; Ali, S.; Chang, L. N.; Brinkley, C.; Turner, K.; Hester, C. *Mater. Lett.* **1990**, 10, 264. (c) Jiang, X. C.; Xie, Y.; Lu, J.; He, W.; Zhu, L. Y.; Qian, Y. T. *J. Mater. Chem.* **2000**, 10, 2193.
- (19) Mann, S. *Angew. Chem., Int. Ed.* **2000**, 39, 3393.
- (20) Liu, J.; Lin, Y. H.; Liang, L.; Voigt, J. A.; Huber, D. L.; Tian, Z. R.; Coker, Mckenzie, E. B.; McDermott, M. J. *Chem.—Eur. J.* **2003**, 9, 605.

- (21) (a) Tang, Q.; Zhou, W. J.; Shen, J. M.; Zhang, W.; Kong, L. F.; Qian, Y. T. *Chem. Commun.* **2004**, 712. (b) Zhang, Z. P.; Shao, X. Q.; Yu, H. D.; Wang, Y. B.; Han, M. Y. *Chem. Mater.* **2005**, *17*, 332.
- (22) (a) Mullin, J. W. *Crystallization*, 3rd ed.; Butterworth-Heinemann: London, 1997; p 248. (b) Xu, L. F.; Guo, Y.; Liao, Q.; Zhang, J. P.; Xu, D. S. *J. Phys. Chem. B* **2005**, *109*, 13519. (c) Wen, X. G.; Zhang, W. X.; Yang, S. H.; Dai, Z. R.; Wang, Z. L. *Nano Lett.* **2002**, *2*, 1397.
- (23) Zhang, L. Z.; Yu, J. C.; Mo, W. M. S.; Li, Q.; Kwong, K. W. *J. Am. Chem. Soc.* **2004**, *126*, 8116.
- (24) Zhang, L. Z.; Ai, Z. H.; Jia, F. L.; Liu, L.; Hu, X. L.; Yu, J. C. *Chem.—Eur. J.* **2006**, *12*, 4185.
- (25) Zhang, L. Z.; Yu, J. C.; Mo, M. S.; Wu, L.; Li, Q.; Kwong, K. W. *Small* **2005**, *1*, 349.
- (26) Bonard, J. M.; Salvétat, J. P.; Stockli, T.; de Heer, W. A.; Forro, L.; Chatelain, A. *Appl. Phys. Lett.* **1998**, *73*, 918.
- (27) Wu, Z. S.; Deng, S. Z.; Xu, N. S.; Chen, J.; Zhou, J.; Chen, J. *Appl. Phys. Lett.* **2002**, *80*, 3829.
- (28) Yin, L. W.; Bando, Y.; Zhu, Y. C.; Li, M. S.; Li, Y. B.; Golberg, D. *Adv. Mater.* **2005**, *17*, 110.
- (29) Chen, J.; Deng, S. Z.; Xu, N. S.; Wang, S. H.; Wen, X. G.; Yang, S. H.; Yang, C. L.; Wang, J. N.; Ge, W. K. *Appl. Phys. Lett.* **2002**, *80*, 3620.
- (30) Li, Y. B.; Bando, Y.; Golberg, D. *Appl. Phys. Lett.* **2003**, *82*, 1962.
- (31) Chueh, Y. L.; Chou, L. J.; Cheng, S. L.; He, J. H.; Wu, W. W.; Chen, L. J. *Appl. Phys. Lett.* **2005**, *86*, 133112.
- (32) Shang, N. G.; Meng, F. Y.; Li, Q.; Lee, C. S.; Lee, S. T. *Adv. Mater.* **2002**, *14*, 1308.
- (33) (a) Lee, C. J.; Lee, T. J.; Lyu, S. C.; Lee, H. J. *Appl. Phys. Lett.* **2002**, *81*, 3648. (b) Tseng, Y. K.; Huang, C. J.; Cheng, H. M.; Liu, K. S.; Chen, I. C. *Adv. Funct. Mater.* **2003**, *13*, 811.
- (34) Li, Y. B.; Bando, Y.; Golberg, D.; Kurashima, K. *Appl. Phys. Lett.* **2002**, *81*, 5048.
- (35) Zhou, J.; Ding, Y.; Deng, S. Z.; Gong, L.; Xu, N. S.; Wang, Z. L. *Adv. Mater.* **2005**, *17*, 2107.
- (36) Chen, C. C.; Yeh, C. C.; Chen, C. H.; Yu, M. Y.; Liu, H. S.; Peng, J. Y.; Chen, Y. F. *J. Am. Chem. Soc.* **2001**, *123*, 2791.
- (37) (a) Tondare, V. N.; Balasubramanian, C.; Shende, S. V.; Godbole, V. P.; Bhorkar, S. V. *Appl. Phys. Lett.* **2002**, *80*, 4813. (b) Tang, Y. B.; Cong, H. T.; Zhao, Z. G.; Cheng, H. M. *Appl. Phys. Lett.* **2005**, *86*, 153104. (c) Tang, Y. B.; Cong, H. T.; Zhao, Z. G.; Cheng, H. M. *Appl. Phys. Lett.* **2005**, *86*, 233104. (d) Shi, S. C.; Chen, C. F.; Chattopadhyay, S.; Chen, K. H.; Chen, L. Y. *Appl. Phys. Lett.* **2005**, *87*, 073109. (e) Liu, C.; Hu, Z.; Wu, Q.; Sang, H.; Deng, S. Z.; Xu, N. S. *J. Am. Chem. Soc.* **2005**, *127*, 1318.
- (38) Filip, V.; Nicolaescu, D.; Tanemura, M.; Okuyama, F. *Ultramicroscopy* **2001**, *89*, 39.
- (39) Gadzuk, J. W.; Plummer, E. W. *Rev. Mod. Phys.* **1973**, *45*, 487.
- (40) Rinzler, A. G.; Hafner, J. H.; Nikolaev, P.; Lou, L.; Kim, S. G.; Tomnek, D.; Nordlander, P.; Colbert, D. T.; Ugarte, D. *Science* **1995**, *269*, 1550.
- (41) Swank, R. K. *Phys. Rev.* **1967**, *153*, 844.
- (42) (a) Nilsson, L.; Groening, O.; Emmenegger, C.; Kuettel, O.; Schaller, E.; Schlapbach, L.; King, H.; Bonard, J. M.; Kern, K. *Appl. Phys. Lett.* **2000**, *76*, 2071. (b) Cao, B. Q.; Teng, X. M.; Heo, S. H.; Li, Y.; Cho, S. O.; Li, G. H.; Cai, W. P. *J. Phys. Chem. C* **2007**, *111*, 2470.
- (43) (a) Li, S. Q.; Liang, Y. X.; Wang, T. H. *Appl. Phys. Lett.* **2005**, *87*, 143104. (b) Jin, C. H.; Wang, J. Y.; Wang, M. S.; Su, J.; Peng, L. M. *Carbon* **2005**, *43*, 1026. (c) Zhou, J.; Xu, N. S.; Deng, S. Z.; Chen, J.; She, J. C.; Wang, Z. L. *Adv. Mater.* **2003**, *15*, 1835.